Exploiting the stereoelectronic effects for selective tuning of band edge states of α-SnO: *GW* quasiparticle calculations

Yabei Wu,[1,2,3] Zhao Tang,[2] Greis J. Cruz,[2] Ya Yang,[4] Wenqing Zhang,[3] Wei Ren,[1,*] and Peihong Zhang[2,†]

[1]*International Centre for Quantum and Molecular Structures, Department of Physics, Shanghai University, 99 Shangda Road, Shanghai 200444, China*

[2]*Department of Physics, University at Buffalo, State University of New York, Buffalo, New York 14260, USA*

[3]*Department of Materials Science and Engineering, Shenzhen Institute for Quantum Science and Engineering, and Academy for Advanced Interdisciplinary Studies, Southern University of Science and Technology, Shenzhen, Guangdong 518055, China*

[4]*Key Laboratory of Microelectronics and Energy of Henan Province, Henan Joint International Research Laboratory of New Energy Storage Technology, Xinyang Normal University, Henan 464000, China*

(Received 22 March 2022; revised 24 June 2022; accepted 20 July 2022; published 1 August 2022)

Tuning the electronic structure of materials, and thus their electronic, transport, and optical properties, is of fundamental importance for materials design and optimization. Although alloying is a well-established method for engineering the band gap of semiconductors, strain engineering has emerged as a promising approach to selective tuning of band-edge states. Using a combined density functional theory and *GW* approach, we show that the highly directional intralayer and interlayer couplings, together with the unusual stereoelectronic effects of the Sn 5s lone pair in α-SnO, may be exploited to tune, in addition to the band gap, the valence and conduction band-edge states selectively using in-plane and/or out-of-plane strains. Whereas the uniaxial strain along the lattice c direction primarily affects the position of the conduction band edge, the valence band edge is very sensitive to the biaxial ab strain. We also establish a strain electronic phase diagram of α-SnO, including the insulator–metal phase transition boundary. It is predicted that a compressive biaxial strain of about 3% or an isotropic pressure of 5 GPa can trigger an insulator–metal transition. The quasiparticle band gap can be widely tuned from 0 to more than 2.0 eV with moderate strains.

DOI: 10.1103/PhysRevB.106.085201

I. INTRODUCTION

Modulating the electronic structure, especially the band-edge states and band gap, of semiconductors to suit targeted applications is a long-term but often challenging problem. Various methods have been proposed—for example, exploiting the strain/lattice mismatch effect [1–3], applying pressure [4,5], doping (or alloying) with isoelectronic elements, or codoping with donor and acceptor pairs [6–8]. Strain engineering, which can be applied in real time (active control) or statically (passive control), has emerged as a promising way to tune the electronic properties of materials. Past efforts have mainly focused on tuning the band gap via lattice strain, and it has been shown that moderate strains can induce indirect–direct or direct–indirect band-gap transitions [9–13], or semiconductor–metal transitions [12,14,15].

There are situations when a semiconductor may have the desired conduction band alignment for certain applications, but the valence band edge may be misaligned, or vice versa. In this case, the performance of a material may benefit greatly from our ability to control selectively the conduction and/or valence band edges. One possibility is to exploit the stereoelectronic properties of certain layered materials to achieve selective tuning of band-edge states, and tin monoxide (also known as α-SnO) is such an example. α-SnO has attracted much research attention recently due to its unusual properties, such as superconductivity under pressure [16–18] and multiferroicity in monolayer SnO [19], and its potential applications in photovoltaics and electronic devices [20–22]. α-SnO assumes a tetragonal PbO layered structure, which can be viewed as a distorted CsCl structure with an elongated c-axis, as shown in Fig. 1. The much-discussed Sn 5s lone pair helps to stabilize the distorted structure with the asymmetric lone-pair electron density projecting out of the layer toward the void region. Interestingly, the Sn 5s lone pair states in α-SnO are not as inert as previously thought, exhibiting a strong hybridization with the O 2p states [23,24]. The *intralayer* hybridization between the O 2p and the Sn lone pair is the defining character of the valence band-edge states of α-SnO. The low-energy conduction states, on the other hand, are derived primarily from the Sn p_x and p_y orbitals, which are sensitive to the *interlayer* Sn–Sn coupling.

In this work, we carry out a systematical study on the strain effects on the electronic structure of α-SnO using density functional theory (DFT) [25,26] and *GW* [27,28] quasiparticle methods. Whereas DFT calculations using the Perdew, Burke, and Ernzerhof (PBE) functional [29] give a band gap of 0.06 eV for the equilibrium structure of α-SnO, our highly converged *GW* calculations predict a band gap of 0.75 eV, which compares very well with the experimental

*renwei@shu.edu.cn
†pzhang3@buffalo.edu

 ©2022 American Physical Society

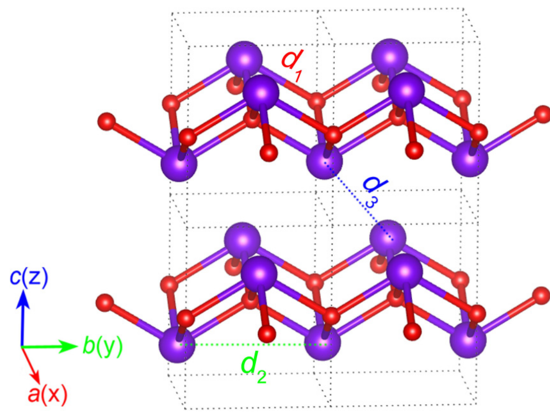

FIG. 1. Crystal structure of α-SnO (space group: *P*4/*nmm*). The large purple spheres are Sn and the small red ones are O atoms. Three important bond lengths (distances) labeled d_1 (Sn—O bond length), d_2 (intralayer Sn–Sn distance), and d_3 (interlayer Sn–Sn distance) are also shown.

gap of 0.70 eV [22]. *GW* calculations for the quasiparticle band structure of α-SnO under various uniaxial and/or biaxial strains are then carried out. We demonstrate that the unusual stereoelectronic effects of α-SnO may be exploited to tune, in addition to the band gap, the valence and conduction band-edge states *selectively* using in-plane and/or out-of-plane strains. We also establish a strain electronic phase diagram and predict a strain-induced semiconductor–metal phase transition boundary of α-SnO. We mention that *GW* calculations of α-SnO under pressure have been reported [17]. Our work is distinguished from that of Chen and Jeng [17] in that, while they focused on the pressure-dependent band gap and pressure-induced superconductivity in SnO, our work elaborates on the distinct roles played by the inter- and intralayer couplings in the selective tuning of the band-edge states. Our work also benefits from the recently developed acceleration *GW* method [30]. Using this method, we are able to include *all* conduction bands in our *GW* calculations at a fraction ($\sim$10%) of computational cost compared with the conventional band-by-band summation approach.

II. COMPUTATIONAL DETAILS

Optimizations of the crystal structures (with or without strains) and DFT electronic structure calculations are carried out using the Vienna Ab initio Simulation Package [31,32]. The energy cutoff for the plane-wave basis set is chosen to be 550 eV. A uniform 8 × 8 × 6 *k*-grid is used for the Brillouin zone integration. Since α-SnO possesses a layered structure, it is important that the van der Waals (vdW) interaction between layers is accurately captured. In this work, we use the vdW-optB86b functional [33] for all structural optimizations. The structures are optimized until forces on all atoms are less than 0.01 eV/Å. The DFT band structures are calculated using the PBE functional [29].

Using the relaxed structures, we then proceed to calculate DFT band structures using the PBE functional [29]. Quasiparticle calculations within the one-shot *GW* (or G^0W^0) approximation are carried out using a local version of the BERKELEYGW package [34], in which the recently developed acceleration method [30] is implemented. The DFT part of the *GW* calculations is carried out using a local version of the PARATEC package [35]. We use the Troullier–Martins norm-conserving pseudopotentials [36] and a high plane-wave cutoff energy of 100 Ry in the DFT part of the *GW* calculations. The high cutoff energy is needed to describe accurately the fairly localized oxygen valence states using norm-conserving pseudopotentials. The Hybertsen–Louie generalized plasmon-pole model [28] is used to extend the static dielectric function to finite frequencies. A Γ-centered *k*-point grid of 8×8×6 is used in our *GW* calculations. This *k*-grid is denser than a 8×8×8 grid for a two-atom cell; such a *k*-grid has been shown to be sufficient to achieve highly converged *GW* band gaps of bulk solids with a small unit cell [37–39]. We mention that *GW* calculations for two-dimensional (2D) materials require a much denser *k*-grid [40–42] due to the analytical behavior of the dielectric function and the electron self-energy in a 2D geometry. Other details of the *GW* calculations will be discussed later.

TABLE I. Comparison between the optimized lattice constants of α-SnO using different functional (PBE and vdW-optB86b) and the experimental values.

	a (Å)	*c* (Å)	*c*/*a*
PBE	3.869	5.036	1.30
vdW-optB86b	3.839	4.804	1.25
Experiment [43]	3.801	4.835	1.27

III. RESULTS AND DISCUSSION

A. DFT electronic structure and chemical features of the band-edge states

α-SnO adopts a tetragonal litharge layered structure (space group *P*4/*nmm*), as shown in Fig. 1. The Sn and O atoms form square pyramids, with Sn atoms at the apexes and O atoms forming the bases, resulting in a sandwiched Sn–O–Sn structure. The hybridization between the active Sn 5*s* lone pair and the O 2*p* states defines the valence band-edges states of α-SnO, and the two-dimensional zigzagging Sn—O bonding network offers various degrees of freedom to tune the intralayer *s*-*p* hybridization as well as the interlayer Sn–Sn interaction. To facilitate later discussion of the strain effects on the structural and electronic properties, we also show in Fig. 1 three bond lengths (distances)—labeled d_1 (Sn—O bond length), d_2 (intralayer Sn–Sn distance), and d_3 (interlayer Sn–Sn distance)—that are important for determining the chemical hybridization, and thus the band-edge positions.

In order to investigate the strain effects on the interlayer Sn–Sn coupling and the hybridization between the stereochemically active Sn 5*s* lone pair and the O 2*p* states, and therefore the low-energy electronic structure of SnO, it is important to establish a theoretical baseline for the equilibrium structure. Table I compares the optimized lattice constants using different functionals and the experimental values [43]. While the PBE functional significantly overestimates both the in-plane and out-of-plane lattice constants, the vdW-optB86b

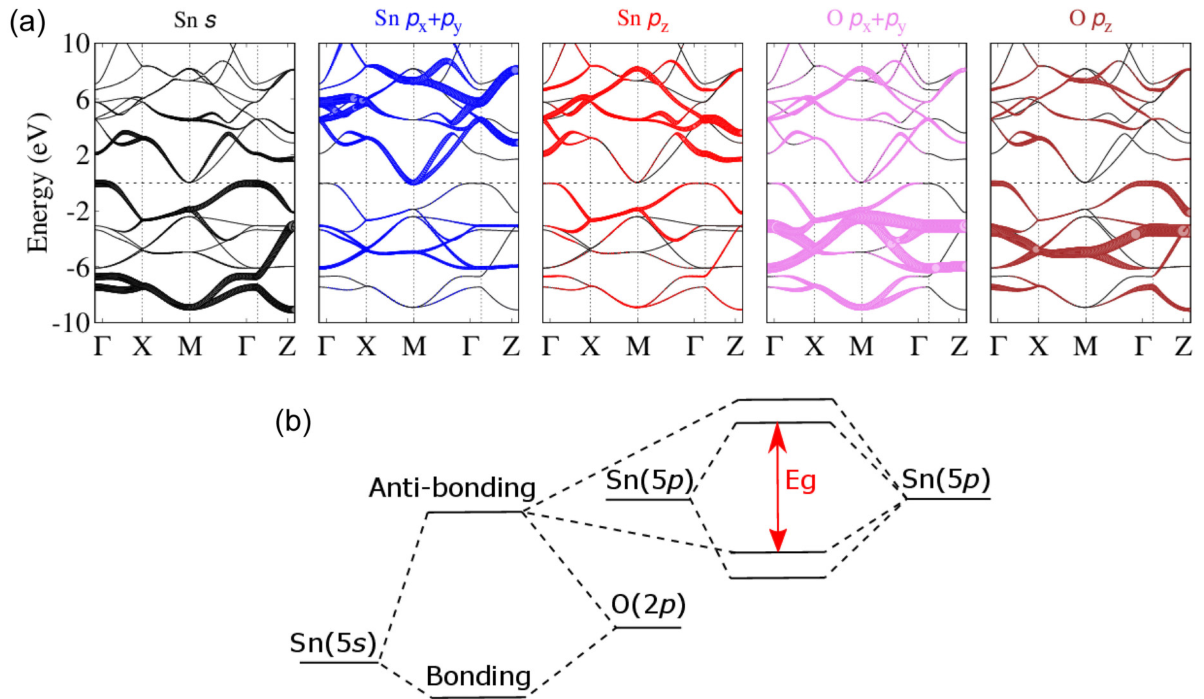

FIG. 2. DFT-PBE band structure and schematic energy-level diagram of α-SnO. (a) DFT band structures showing the decomposition of the band wave functions into contributions from different atomic orbitals. (b) Schematic energy-level diagrams for better understanding the overall band structure and the strain effects on the band-edge states.

functional [33] predicts lattice constants to within 1% accuracy compared with the experiment, indicating the importance of including the vdW interaction in theoretical calculations of layered materials. Our results are also consistent with previous theoretical work [44]. Therefore, we will use structures optimized with the vdW-optB86b functional (with or without strains) for electronic structure calculations.

Figure 2(a) shows the DFT band structure projected onto contributions from different atomic characters. The stereochemically active lone-pair (Sn 5s) states strongly hybridize with the oxygen p states and contribute significantly to the top valence states. As a result, whereas the low-energy valence bands are mostly derived from the Sn 5s states, the top valence band also acquires significant Sn 5s character through the hybridization with O p_z orbitals. As expected, low-energy conduction bands are predominantly of the Sn 5p character, and the conduction band minimum (CBM) states (at the M point) are mostly derived from Sn $5p_x + 5p_y$. The strong dispersion of the lowest conduction bands around the M point comes primarily from the interlayer Sn–Sn coupling. Therefore, the CBM and valence band maximum (VBM) states have distinct atomic characters and orbital orientations. This suggests that they may respond differently to lattice strains along different directions: Whereas the VBM states should be sensitive to in-plane strains, the CBM state may be more susceptible to strains along the lattice c direction, providing a practical means to tune the CBM and VBM states separately through lattice strains. The overall band structure can be schematically understood using the energy diagram shown in Fig. 2(b), which also helps understand the strain effects on the electronic structure of α-SnO, as discussed later. The strong hybridization between the Sn 5s and O 2p states gives rise to the bonding and antibonding states, which defines the main characters of the top and bottom of the valence bands. This understanding is consistent with the projected band structure shown in Fig. 2(a). The antibonding states then further hybridize with the Sn 5p states, which ultimately determine the band-edge electronic structure. This energy diagram is also consistent with the revised lone-pair model proposed by Walsh *et al.* [23,24].

It should be mentioned that the dispersion of the top valence band appears to be very flat near the Γ point. Upon a more careful inspection, the VBM actually shifts slightly away from the Γ point to $k \approx [0.075, 0.075, 0.0]2\pi/a$. The VBM is only about 8 meV higher than the band energy at the Γ point, resulting in a warped Mexican-hat–like band dispersion in the xy plane. This Mexican-hat band dispersion is more pronounced for the monolayer structure [19]. Within DFT-PBE, the calculated direct band gap at the Γ point is 2.13 eV, and that at the M point is 1.99 eV; the $\Gamma \rightarrow M$ indirect gap calculated within PBE is 0.063 eV, whereas the minimum indirect gap is about 0.055 eV. Not surprisingly, the PBE results for the band gaps are significantly smaller than the experimental values [22] of about 0.7 eV (minimum indirect gap) and 2.7 eV (direct gap). Higher level many-body perturbation calculations within the GW approximation can bring the results much closer to the experiment. In addition, after including the quasiparticle self-energy correction, the VBM state also shifts to the Γ point, as discussed next.

B. Quasiparticle band structure of α-SnO

The DFT results presented in the previous section provide an important understanding of the overall electronic

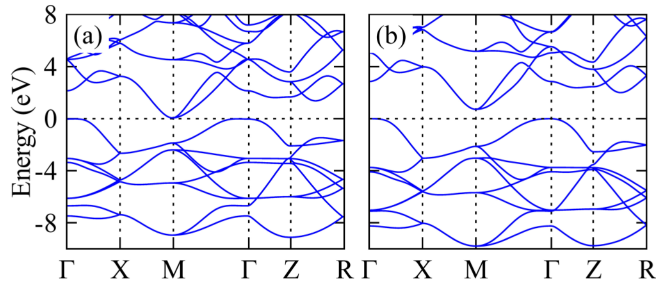

FIG. 3. Band structure of α-SnO calculated using (a) the DFT-PBE method and (b) the *GW* approximation. The VBM is set to zero.

structure of α-SnO. However, neither the band dispersion nor the fundamental band gap predicted within the DFT approach is accurate. On the other hand, first-principles calculations based on many-body perturbation theory within the *GW* approximation [27,28] are very successful in predicting the quasiparticle properties of solids. Therefore, before we investigate the strain effects on the electronic structure of α-SnO, we would like to discuss briefly its quasiparticle band structure calculated within the *GW* approximation.

Figure 3 compares the DFT-PBE and *GW* band structures of α-SnO. As we mentioned earlier, DFT-PBE calculations predict a Mexican-hat–like dispersion for the top valence band, and the VBM slightly shifts away from the Γ point. After including the *GW* self-energy corrections, the VBM is predicted to be at the Γ point. In other words, there is no Mexican-hat–like dispersion for the top valence band within the *GW* approximation. The valence bandwidth is also increased from 9.03 eV (PBE) to 9.57 eV (*GW*). Our highly converged *GW* calculations give an indirect band gap of 0.75 eV (Γ-*M*), which is very close to the experimental band gap of about 0.70 eV [22], especially considering that experimental results include the temperature effects. The calculated direct quasiparticle band gaps are 2.78 eV (at the *M* point) and 2.84 eV (at Γ); these results again agree well with the experimental results, ranging from 2.70 eV [22] to 2.85 eV [20]. A summary of the calculated band gaps and their comparison with the experiment is presented in Table II.

Before concluding this section, we briefly discuss the convergence issue of quasiparticle calculations within the *GW* approximation. *GW* calculations are known to be particularly difficult to converge for oxide materials [30,34,45–47] due to the contrasting wave function characters of the valence and conduction bands. Whereas the valence bands are derived from fairly localized oxygen *p* states, conduction bands are primarily from cation *s* and/or *p* states, which are often rather delocalized. Within the conventional first-principles *GW* approach [28,34], there are two interrelated convergence parameters: the kinetic energy cutoff (E_{cut}) for the dielectric matrix and the number of conduction bands (N_c) included in the calculations of the dielectric matrix and the Coulomb-hole self-energy. The more localized the quasiparticle wave functions are, the higher cutoff energy and more conduction bands are required for an accurate account of the correlation effects [45].

TABLE II. Summary of the theoretical band gaps (in electron volts) calculated within DFT-PBE and the *GW* approximation, and their comparison with the experiment.

	Indirect gap (Γ–*M*)	Direct gap (*M*)	Direct gap (Γ)
PBE	0.06	1.99	2.13
GW	0.75	2.78	2.84
Experiment [43]	0.70 [22]	2.70 ∼ 2.85 [22]	

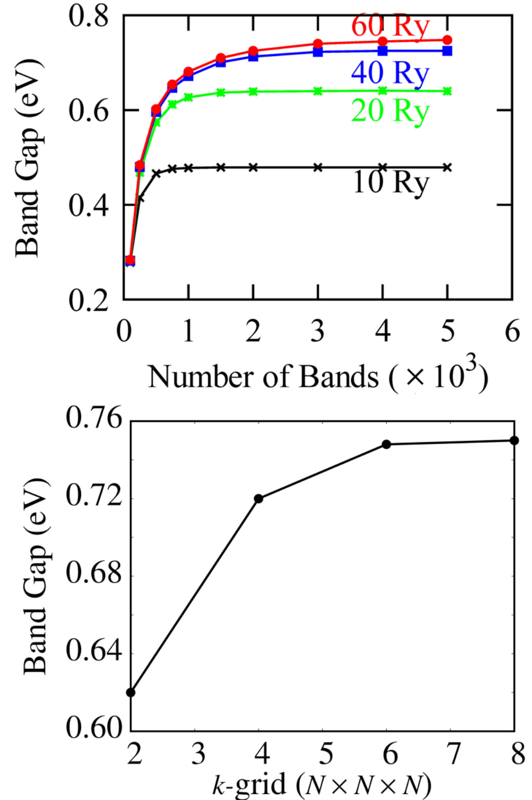

FIG. 4. Convergence behavior of the calculated indirect quasiparticle band gap of α-SnO: (top panel) with respect to the number of bands included in the *GW* calculations and the cutoff energy of the dielectric matrix, and (bottom panel) with respect to the *k*-grid density.

The top panel of Fig. 4 shows the calculated minimum indirect quasiparticle band gap (Γ−M) as a function of E_{cut} and N_c. It is clear that a high cutoff energy of about 60 Ry for the dielectric matrix is required to converge the calculated quasiparticle energies. In addition, a fairly large number (about 4000, or 1000/atom) of conduction bands is needed to fully converge the band gap. Using our recently developed methods [30,48], in which the conventional band-by-band summation is replaced with an energy integration technique, we are able to include *all* conduction bands effectively in the calculation of the dielectric matrix and the Coulomb hole self-energy at a fraction (less than 10%, in this case) of the computational cost compared with the conventional approach. Although there are previous works [17,44] on *GW* calculations of α-SnO, our work clearly demonstrates the importance of the convergence issue since underconverged calculations may give inaccurate predictions. It is well understood that *GW* results typically

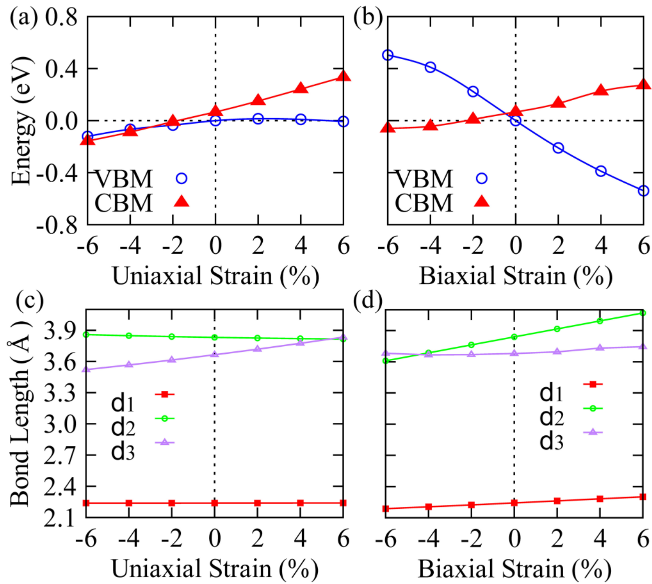

FIG. 5. Strain effects on the band edge positions (a) and (b), and on the relevant bond lengths (c) and (d) of α-SnO. The band structures calculated at different strains are aligned using the O 1s core level as a reference. The bond lengths (distances) d_1, d_2, and d_3 are defined in Fig. 1.

converge quickly with respect to the k-grid density. Nevertheless, we show in the bottom panel of Fig. 4 the calculated *GW* band gap with respect to the k-grid density; a $6 \times 6 \times 6$ k-grid would be sufficient to converge the band gap to within 0.01 eV.

C. Exploiting the stereoelectronic effects to tune selectively the band-edge states, and the strain phase diagram of α-SnO

The distinct atomic origins and spatial orientations of the VBM and CBM states, as shown in Fig. 2, offer a practical means for selectively tuning the band edge states with uniaxial and/or biaxial strains. The dispersion of the lowest conduction band, thus the position of the CBM state, is primarily determined by the interlayer coupling between the Sn 5p states, as shown in Fig. 2. The VBM position, on the other hand, is mainly determined by the bonding–antibonding splitting, which in turn is a result of the intralayer hybridization between the stereochemically active Sn 5s lone pair and the O 2p valence states (see Fig. 2). These observations suggest that the CBM position may be tuned by the uniaxial c strain (ε_c), whereas the VBM may be more sensitive to the biaxial ab strain (ε_{ab}).

The top panels of Fig. 5 show the shifts in the VBM and CBM energies in response to ε_c [Fig. 5(a)] and ε_{ab} [Fig. 5(b)], calculated within DFT. We use the O 1s core state as a reference to align the band structures calculated with different strains. First, the CBM position shifts upward with the uniaxial strain along the c direction, as shown in Fig. 5(a). This is expected since the interlayer Sn–Sn coupling, which is one of the main contributions to the dispersion of the lowest conduction band, becomes weaker with increasing ε_c. The VBM position, on the other hand, is minimally affected by the uniaxial tensile strain, but shifts slightly lower with increasing compressive strain. We have also tested results calculated using the Sn 4s semicore state as a reference and do not observe any noticeable differences.

The strain-dependent VBM and CBM positions are consistent with our understanding of the strain effects on the coupling between atomic orbitals. Figure 5(c) shows three relevant bond lengths (atomic separations), labeled d_1 (intralayer Sn—O bond length), d_2 (intralayer Sn–Sn distance), and d_3 (interlayer Sn–Sn distance), as a function of ε_c (see also Fig. 1). The reduced interlayer Sn–Sn interaction (as a result of elongated d_3) with increasing ε_c is mainly responsible for the upward shift of the CBM position shown in Fig. 5(a). The small decrease in the intralayer Sn–Sn distance (d_2) with increasing ε_c, however, has an opposite effect on the CBM position. The subtle shift in the VBM position with the compressive strain ε_c can also be understood: Although the intralayer Sn—O bond (d_1) does not change appreciably with ε_c due to the rigidity of the bonds, the Sn—O—Sn bond angle is substantially affected by the compressive uniaxial strain ε_c, which results in a slight decrease in the bonding–antibonding splitting, as shown schematically in Fig. 2(b), therefore lowing the VBM position.

The results are very different for the biaxial strain ε_{ab}: Whereas the VBM moves downward with increasing ε_{ab}, the CBM position moves upward at a much lower rate compared with that of the downward movement of the VBM position. These results can again be understood by inspecting the

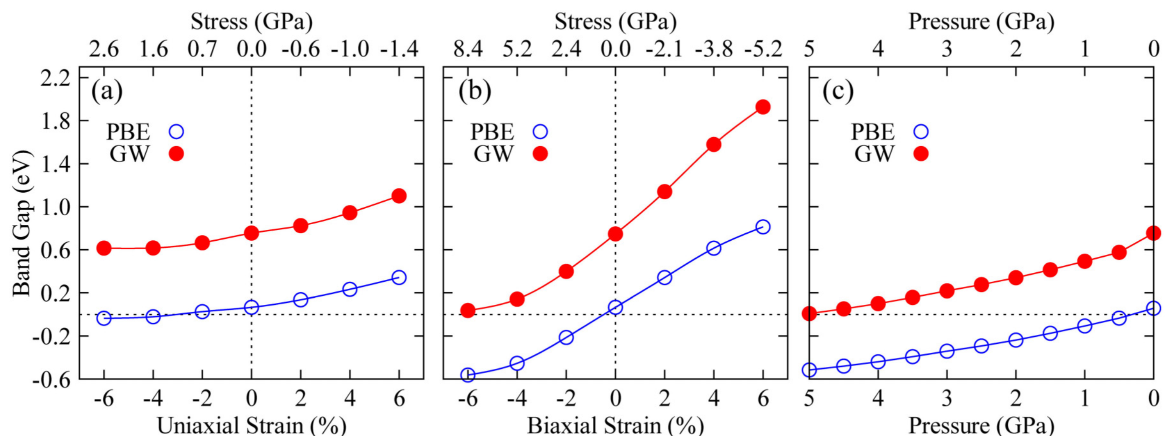

FIG. 6. Engineering the band gap of α-SnO via (a) uniaxial strain, (b) biaxial strain, and (c) isotropic pressure.

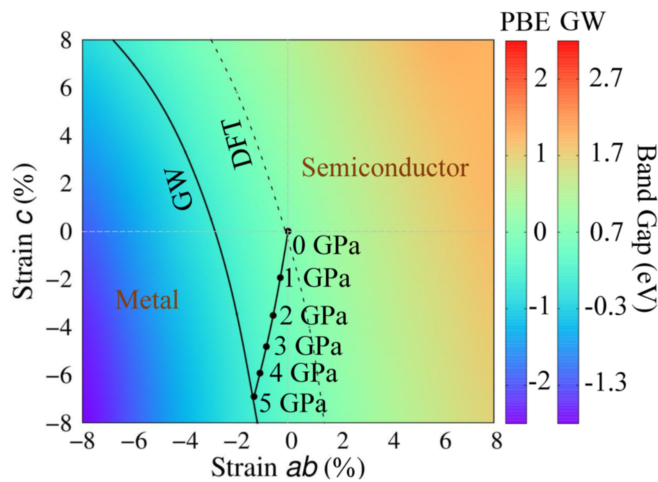

FIG. 7. Strain phase diagram of α-SnO predicted by the DFT-PBE and *GW* methods.

variation of d_1, d_2, and d_3 with ε_{ab}, as shown in Fig. 5(d). As mentioned earlier [see also Fig. 2(b)], the VBM energy is largely determined by the bonding–antibonding splitting as a result of the hybridization between the Sn 5*s* lone pair and the O 2*p* valence states. In this case, the intralayer Sn—O bond length d_1 increases linearly with ε_{ab}, as expected. The elongated Sn—O bonds then result in a reduced bonding–antibonding splitting, therefore lowering the position of the VBM state. The upward shift in the CBM position with increasing ε_{ab} can be largely attributed to the increasing intralayer Sn–Sn distance d_2, since the dispersion of the lowest conduction band—and thus the CBM position—is mostly determined by the coupling between the $p_x + p_y$ orbitals of neighboring Sn atoms, as illustrated in Fig. 2.

With these results at hand, we now proceed to investigate strain or pressure engineering of the band gap of α-SnO. The DFT results shown earlier, however, suffer from the well-known band-gap problem, and therefore cannot provide accurate predictions of the band gap or the electronic structure phase transitions under strain. We have carried out *GW* calculations for all strained structures. Figure 6(a) and 6(b) show the calculated *GW* bang gap of α-SnO under uniaxial and biaxial strains. The band gap increases with both strains, although the biaxial strain is far more effective than the uniaxial strain for tuning the band gap. A moderate 4% biaxial strain would be sufficient to increase the band gap of α-SnO from 0.75 eV at equilibrium to 1.6 eV, and the band gap can be widely tuned from 0 to over 2.0 eV within ±6% biaxial strains. Figure 6(c) shows the dependence of the calculated band gaps on the (isotropic) pressure. The band gap decreases monotonically with increasing isotropic pressure. Our *GW* calculations suggest that a 5-GPa isotropic pressure may trigger an insulator–metal transition in α-SnO; this result agrees very well with experimental reports [16,49].

Finally, we present in Fig. 7 the strain electronic phase diagram of α-SnO. The color map shows the calculated band gap using the DFT-PBE and *GW* approaches. A widely tunable band gap from 0 to 3 eV can be achieved with the combination of strains. The dashed curve indicates the metal–insulator phase boundary predicted by DFT-PBE, whereas the solid curve is predicted by the *GW* method. The strains induced by the isotropic pressures are shown with the solid curve with black dots. Although the uniaxial strain ε_c can somewhat modulate the band gap, biaxial strain ε_{ab} is much more effective in doing so. The combination of both strains offers ample possibilities to tune the low-energy electronic properties, in addition to the band gap, or to produce a metal–insulator transition in α-SnO.

IV. SUMMARY

In summary, we have systematically investigated the strain effects on the electronic properties of α-SnO—in particular, the band-edge states and the band gap—using DFT and *GW* quasiparticle calculations. Our highly converged *GW* calculations predict an indirect gap of 0.75 eV, which agrees well with the experimental value of 0.70 eV and ensures accurate predictions of the strain-dependent electronic structure. We find the VBM and CBM states are derived from distinct atomic orbitals and respond disparately to strains along different directions. Such stereoelectronic effects can be exploited to tune the VBM and CBM states selectively, and therefore the band gap, via different strains. Theoretical results can be understood by analyzing the strain effects on the coupling of relevant atomic orbitals. We have also established a strain electronic phase diagram and the semiconductor–metal transition boundary of α-SnO under combinations of out-of-plane and in-plane strains. The predicted phase transition under pressure by the *GW* method also agrees well with experiments.

ACKNOWLEDGMENTS

This work is supported in part by the National Natural Science Foundation of China (Grants No. 12104207 and No. 11929401). Work at UB is supported by the US-NSF under Grants No. DMR-1506669 and No. DMREF-1626967. P.Z. acknowledges the Southern University of Science and Technology of China and the Shanghai University for supporting his extended visits while on sabbatical, during which part of this work was done. We acknowledge the computational support provided by the Center for Computational Science and Engineering at Southern University of Science and Technology and the Center for Computational Research at UB.

[1] Z. Zhang, L. Li, J. Horng, N. Z. Wang, F. Yang, Y. Yu, Y. Zhang, G. Chen, K. Watanabe, T. Taniguchi, X. H. Chen, F. Wang, and Y. Zhang, Strain-modulated bandgap and piezo-resistive effect in black phosphorus field-effect transistors, Nano Lett. **17**, 6097 (2017).

[2] V. R. D'Costa, Y. Y. Fang, J. Tolle, J. Kouvetakis, and J. Menendez, Tunable Optical Gap at a Fixed Lattice Constant in Group-IV Semiconductor Alloys, Phys. Rev. Lett. **102**, 107403 (2009).

[3] K. He, C. Poole, K. F. Mak, and J. Shan, Experimental demonstration of continuous electronic structure tuning

via strain in atomically thin MoS_2, Nano Lett. **13**, 2931 (2013).

[4] N. E. Christensen, A. Svane, and E. L. Peltzer y Blancá, Electronic and structural properties of SnO under pressure, Phys. Rev. B **72**, 014109 (2005).

[5] A. P. Nayak, S. Bhattacharyya, J. Zhu, J. Liu, X. Wu, T. Pandey, C. Jin, A. K. Singh, D. Akinwande, and J. F. Lin, Pressure-induced semiconducting to metallic transition in multilayered molybdenum disulphide, Nat. Commun. **5**, 3731 (2014).

[6] W. Zhu, X. Qiu, V. Iancu, X. Q. Chen, H. Pan, W. Wang, N. M. Dimitrijevic, T. Rajh, H. M. Meyer 3rd, M. P. Paranthaman, G. M. Stocks, H. H. Weitering, B. Gu, G. Eres, and Z. Zhang, Band Gap Narrowing of Titanium Oxide Semiconductors by Noncompensated Anion-Cation Codoping for Enhanced Visible-Light Photoactivity, Phys. Rev. Lett. **103**, 226401 (2009).

[7] Y. Gai, J. Li, S. S. Li, J. B. Xia, and S. H. Wei, Design of Narrow-Gap TiO_2: A Passivated Codoping Approach for Enhanced Photoelectrochemical Activity, Phys. Rev. Lett. **102**, 036402 (2009).

[8] H. Kato and A. Kudo, Visible-light-response and photocatalytic activities of TiO_2 and $SrTiO_3$ photocatalysts codoped with antimony and chromium, J. Phys. Chem. B **106**, 5029 (2002).

[9] A. S. Rodin, A. Carvalho, and A. H. Castro Neto, Strain-Induced Gap Modification in Black Phosphorus, Phys. Rev. Lett. **112**, 176801 (2014).

[10] F. Zhang, V. H. Crespi, and P. Zhang, Prediction That Uniaxial Tension Along $\langle 111 \rangle$ Produces a Direct Band Gap in Germanium, Phys. Rev. Lett. **102**, 156401 (2009).

[11] S. B. Desai, G. Seol, J. S. Kang, H. Fang, C. Battaglia, R. Kapadia, J. W. Ager, J. Guo, and A. Javey, Strain-induced indirect to direct bandgap transition in multilayer WSe_2, Nano Lett. **14**, 4592 (2014).

[12] N. Lu, H. Guo, L. Li, J. Dai, L. Wang, W. N. Mei, X. Wu, and X. C. Zeng, MoS_2/MX_2 heterobilayers: Bandgap engineering via tensile strain or external electrical field, Nanoscale **6**, 2879 (2014).

[13] Y. Wu, W. Xia, W. Gao, W. Ren, and P. Zhang, Engineering the Near-Edge Electronic Structure of SnSe Through Strains, Phys. Rev. Appl. **8**, 034007 (2017).

[14] Z. H. Ni, T. Yu, Y. H. Lu, Y. Y. Wang, Y. P. Feng, and Z. X. Shen, Uniaxial strain on graphene: Raman spectroscopy study and band-gap opening, ACS Nano **2**, 2301 (2008).

[15] D.- B. Zhang and S.- H. Wei, Inhomogeneous strain-induced half-metallicity in bent zigzag graphene nanoribbons, npj Comput. Mater. **3**, 32 (2017).

[16] M. K. Forthaus, K. Sengupta, O. Heyer, N. E. Christensen, A. Svane, K. Syassen, D. I. Khomskii, T. Lorenz, and M. M. Abd-Elmeguid, Superconductivity in SnO: A Nonmagnetic Analog to Fe-Based Superconductors?, Phys. Rev. Lett. **105**, 157001 (2010).

[17] P. J. Chen and H. T. Jeng, Phase diagram of the layered oxide SnO: GW and electron-phonon studies, Sci. Rep. **5**, 16359 (2015).

[18] J. Zhang, Y. Han, C. Liu, W. Ren, Y. Li, Q. Wang, N. Su, Y. Li, B. Ma, Y. Ma, and C. Gao, Electrical transport properties of SnO under high pressure, J. Phys. Chem. C **115**, 20710 (2011).

[19] L. Seixas, A. S. Rodin, A. Carvalho, and A. H. Castro Neto, Multiferroic Two-Dimensional Materials, Phys. Rev. Lett. **116**, 206803 (2016).

[20] K. J. Saji, K. Tian, M. Snure, and A. Tiwari, 2D Tin monoxide: An unexplored *p*-type van der Waals semiconductor: Material characteristics and field effect transistors, Adv Electron Mater **2**, 1500453 (2016).

[21] F. Zhang, J. Zhu, D. Zhang, U. Schwingenschlogl, and H. N. Alshareef, Two-dimensional SnO anodes with a tunable number of atomic layers for sodium ion batteries, Nano Lett. **17**, 1302 (2017).

[22] Y. Ogo, H. Hiramatsu, K. Nomura, H. Yanagi, T. Kamiya, M. Hirano, and H. Hosono, *p*-Channel thin-film transistor using *p*-type oxide semiconductor, SnO, Appl. Phys. Lett. **93**, 032113 (2008).

[23] A. Walsh and G. W. Watson, Influence of the anion on lone pair formation in Sn(II) monochalcogenides: A DFT study, J. Phys. Chem. B **109**, 18868 (2005).

[24] A. Walsh, D. J. Payne, R. G. Egdell, and G. W. Watson, Stereochemistry of post-transition metal oxides: Revision of the classical lone pair model, Chem. Soc. Rev. **40**, 4455 (2011).

[25] P. Hohenberg and W. Kohn, Inhomogeneous electron gas, Phys. Rev. **136**, B864 (1964).

[26] W. Kohn and L. J. Sham, Self-consistent equations including exchange and correlation effects, Phys. Rev. **140**, A1133 (1965).

[27] L. Hedin, New method for calculating the one-particle green's function with application to the electron-gas problem, Phys. Rev. **139**, A796 (1965).

[28] M. S. Hybertsen and S. G. Louie, Electron correlation in semiconductors and insulators: Band gaps and quasiparticle energies, Phys. Rev. B **34**, 5390 (1986).

[29] J. P. Perdew, K. Burke, and M. Ernzerhof, Generalized Gradient Approximation Made Simple, Phys. Rev. Lett. **77**, 3865 (1996).

[30] W. Gao, W. Xia, X. Gao, and P. Zhang, Speeding up GW calculations to meet the challenge of large scale quasiparticle predictions, Sci. Rep. **6**, 36849 (2016).

[31] G. Kresse and J. Hafner, Ab initio molecular dynamics for liquid metals, Phys. Rev. B **47**, 558 (1993).

[32] G. Kresse and J. Furthmuller, Efficiency of ab-initio total energy calculations for metals and semiconductors using a plane-wave basis set, Comp. Mater. Sci. **6**, 15 (1996).

[33] J. Klimeš, D. R. Bowler, and A. Michaelides, van der Waals density functionals applied to solids, Phys. Rev. B **83**, 195131 (2011).

[34] J. Deslippe, G. Samsonidze, D. A. Strubbe, M. Jain, M. L. Cohen, and S. G. Louie, BerkeleyGW: A massively parallel computer package for the calculation of the quasiparticle and optical properties of materials and nanostructures, Comput. Phys. Commun. **183**, 1269 (2012).

[35] B. G. Pfrommer, J. Demmel, and H. Simon, Unconstrained energy functionals for electronic structure calculations, J. Comput. Phys. **150**, 287 (1999).

[36] N. Troullier and J. L. Martins, Efficient pseudopotentials for plane-wave calculations, Phys. Rev. B **43**, 1993 (1991).

[37] Z. Ergönenc, B. Kim, P. Liu, G. Kresse, and C. Franchini, Converged GW quasiparticle energies for transition metal oxide perovskites, Phys. Rev. Mater. **2**, 024601 (2018) .

[38] H. Cao, Z. Yu, P. Lu, and L.- W. Wang, Fully converged plane-wave-based self-consistent GW calculations of periodic solids, Phys. Rev. B **95**, 035139 (2017).

[39] T. Rangel, M. Del Ben, D. Varsano, G. Antonius, F. Bruneval, F. H. da Jornada, M. J. van Setten, O. K. Orhan, D. D. O'Regan, A.

Canning, A. Ferretti, A. Marini, G.- M. Rignanese, J. Deslippe, S. G. Louie, and J. B. Neaton, Reproducibility in G0W0 calculations for solids, Comput. Phys. Commun. **255**, 107242 (2020).

[40] F. A. Rasmussen, P. S. Schmidt, K. T. Winther, and K. S. Thygesen, Efficient many-body calculations for two-dimensional materials using exact limits for the screened potential: Band gaps of MoS_2 *h*-BN, and phosphorene, Phys. Rev. B **94**, 155406 (2016).

[41] F. H. da Jornada, D. Y. Qiu, and S. G. Louie, Nonuniform sampling schemes of the Brillouin zone for many-electron perturbation-theory calculations in reduced dimensionality, Phys. Rev. B **95**, 035109 (2017).

[42] W. Xia, W. Gao, G. Lopez-Candales, Y. Wu, W. Ren, W. Zhang, and P. Zhang, Combined subsampling and analytical integration for efficient large-scale GW calculations for 2D systems, npj Comput. Mater. **6**, 118 (2020).

[43] M. S. Moreno and R. C. Mercader, Mössbauer study of SnO lattice dynamics, Phys. Rev. B **50**, 9875 (1994).

[44] K. Govaerts, R. Saniz, B. Partoens, and D. Lamoen, van der Waals bonding and the quasiparticle band structure of SnO from first principles, Phys. Rev. B **87**, 235210 (2013).

[45] B. C. Shih, Y. Xue, P. Zhang, M. L. Cohen, and S. G. Louie, Quasiparticle Band Gap of ZnO: High Accuracy from the Conventional G(0)W(0) Approach, Phys. Rev. Lett. **105**, 146401 (2010).

[46] C. Friedrich, M. C. Müller, and S. Blügel, Band convergence and linearization error correction of all-electron ***GW*** calculations: The extreme case of zinc oxide, Phys. Rev. B **83**, 081101(R) (2011).

[47] G. Lopez-Candales, Z. Tang, W. Xia, F. Jia, and P. Zhang, Quasiparticle band structure of $SrTiO_3$ and $BaTiO_3$: A combined LDA+U and G_0W_0 approach, Phys. Rev. B **103**, 035128 (2021).

[48] W. Gao, W. Xia, Y. Wu, W. Ren, X. Gao, and P. Zhang, Quasiparticle band structures of CuCl, CuBr, AgCl, and AgBr: The extreme case, Phys. Rev. B **98**, 045108 (2018).

[49] X. Wang, F. X. Zhang, I. Loa, K. Syassen, M. Hanfland, and Y. L. Mathis, Structural properties, infrared reflectivity, and Raman modes of SnO at high pressure, Phys. Status Solidi B **241**, 3168 (2004).